PNAS RESEARCH ARTICLE | EARTH, ATMOSPHERIC, AND PLANETARY SCIENCES

The origin of carbonate mud and implications for global climate

Emily C. Geyman[a,b,1], Ziman Wu[c], Matthew D. Nadeau[b], Stacey Edmonsond[b,d], Andrew Turner[c], Sam J. Purkis[e], Bolton Howes[b], Blake Dyer[d], Anne-Sofie C. Ahm[b,d], Nan Yao[f], Curtis A. Deutsch[b], John A. Higgins[b], Daniel A. Stolper[c], and Adam C. Maloof[b]

Edited by Patricia Dove, Virginia Polytechnic Institute and State University, Blacksburg, VA; received June 20, 2022; accepted September 1, 2022

Carbonate mud represents one of the most important geochemical archives for reconstructing ancient climatic, environmental, and evolutionary change from the rock record. Mud also represents a major sink in the global carbon cycle. Yet, there remains no consensus about how and where carbonate mud is formed. Here, we present stable isotope and trace-element data from carbonate constituents in the Bahamas, including ooids, corals, foraminifera, and algae. We use geochemical fingerprinting to demonstrate that carbonate mud cannot be sourced from the abrasion and mixture of any combination of these macroscopic grains. Instead, an inverse Bayesian mixing model requires the presence of an additional aragonite source. We posit that this source represents a direct seawater precipitate. We use geological and geochemical data to show that "whitings" are unlikely to be the dominant source of this precipitate and, instead, present a model for mud precipitation on the bank margins that can explain the geographical distribution, clumped-isotope thermometry, and stable isotope signature of carbonate mud. Next, we address the enigma of why mud and ooids are so abundant in the Bahamas, yet so rare in the rest of the world: Mediterranean outflow feeds the Bahamas with the most alkaline waters in the modern ocean (>99.7th-percentile). Such high alkalinity appears to be a prerequisite for the nonskeletal carbonate factory because, when Mediterranean outflow was reduced in the Miocene, Bahamian carbonate export ceased for 3-million-years. Finally, we show how shutting off and turning on the shallow carbonate factory can send ripples through the global climate system.

Bahamas | carbonates | geochemistry | pCO_2 | climate

Significance

The Bahama Banks produce huge volumes of carbonate mud. These sediments represent a major sink in the modern carbon cycle, and likely an even larger sink in the ancient carbon cycle. Yet, it is still debated where and how carbonate mud is formed. We use geochemical fingerprinting to show that mud cannot be derived from the breakdown and mixing of any combination of known carbonate grains or skeletal sources. Rather, mud represents a distinct seawater precipitate. We use ancient sedimentary and modern oceanographic evidence to show that high seawater alkalinity is required to produce carbonate mud. Finally, we illustrate how the size and strength of the shallow carbonate factory plays a first-order control in setting global pCO_2 and climate.

Carbonate mud has been an important constituent of the sedimentary rock record for the last 3.5 billion years of Earth history (1). Carbonate mud represents both a major sink in the geological carbon cycle (2, 3) and one of the principal sedimentary archives for reconstructing ancient seawater chemistry and climate (4–6). However, the fact that we still lack an understanding of how and where mud forms on Earth today (7–9) presents a challenge to the interpretation of the geochemical records of ancient muds. For example, modern observations indicate that the varied carbonate constituents within a handful of sediment may exhibit as much geochemical variability as carbonates spanning the last billion years of Earth history (10). Thus, constraining the origin of modern carbonate mud can help us account for the processes that cause the geochemistry of these carbonates to differ from that of coeval global ocean water (10–14), and guide us to convert our laboratory measurements of ancient muds into more accurate records of past environmental change.

The origin of carbonate mud (particle diameter <63 μm) remains one of the longstanding unanswered questions in sedimentology. The Great Bahama Bank (GBB), an isolated carbonate platform that is dominated by nonskeletal sands and muds (15–17), has been at the center of the debate for over a century (8, 18–24). Broadly, there are three prevailing hypotheses for mud formation. First, carbonate mud could be formed by algae (7, 20, 25). This hypothesis is supported by observations that algae secrete aragonite needles with similar morphologies (20) and $\delta^{18}O$ values (7) as banktop mud. Second, mud could form via direct precipitation from the water column during so-called "whiting events" (22–24), whereby fine-grained carbonate particles fill the water column, giving it a milky white appearance (21). Finally, the abrasion of ooids (9), intraclasts, and skeletal grains (26–29) could represent a source of fine-grained carbonate.

Most existing models for mud formation are challenged by at least one line of evidence. For example, 1) the old radiocarbon signature of suspended aragonite needles in whiting events (30, 31) and 2) the lack of a drop in alkalinity in active whiting waters (8, 21, 30) both indicate that whitings are more likely to represent the resuspension of existing fine-grained sediment than the pseudohomogenous precipitation of new particles (8, 31). Additionally, while the "whiting zone" has a relatively narrow geographic extent west of Andros Island (22–24, 32), all of the basins surrounding the Bahama Banks are covered by thick blankets of carbonate mud (33–35), suggesting that mud is being

Author affiliations: [a]Division of Geological and Planetary Sciences, California Institute of Technology, Pasadena, CA 91125; [b]Department of Geosciences, Princeton University, Princeton, NJ 08544; [c]Department of Earth and Planetary Science, University of California, Berkeley, CA 94720; [d]Department of Earth and Ocean Sciences, University of Victoria, Victoria, BC V8P 5C2, Canada; [e]Department of Marine Geosciences, Rosenstiel School of Marine and Atmospheric Science, University of Miami, Miami, FL 33149; and [f]Princeton Institute for the Science and Technology of Materials, Princeton University, Princeton, NJ 08544

Author contributions: E.C.G. and A.C.M. designed research; E.C.G., Z.W., M.D.N., S.E., A.T., S.J.P., B.H., B.D., A.-S.C.A., N.Y., C.A.D., J.A.H., D.A.S., and A.C.M. performed research; E.C.G. analyzed data; and E.C.G. and A.C.M. wrote the paper.

The authors declare no competing interest.

This article is a PNAS Direct Submission.

See online for related content such as Commentaries.

[1]To whom correspondence may be addressed. Email: egeyman@caltech.edu.

This article contains supporting information online at https://www.pnas.org/lookup/suppl/doi:10.1073/pnas.2210617119/-/DCSupplemental.

Published October 17, 2022.

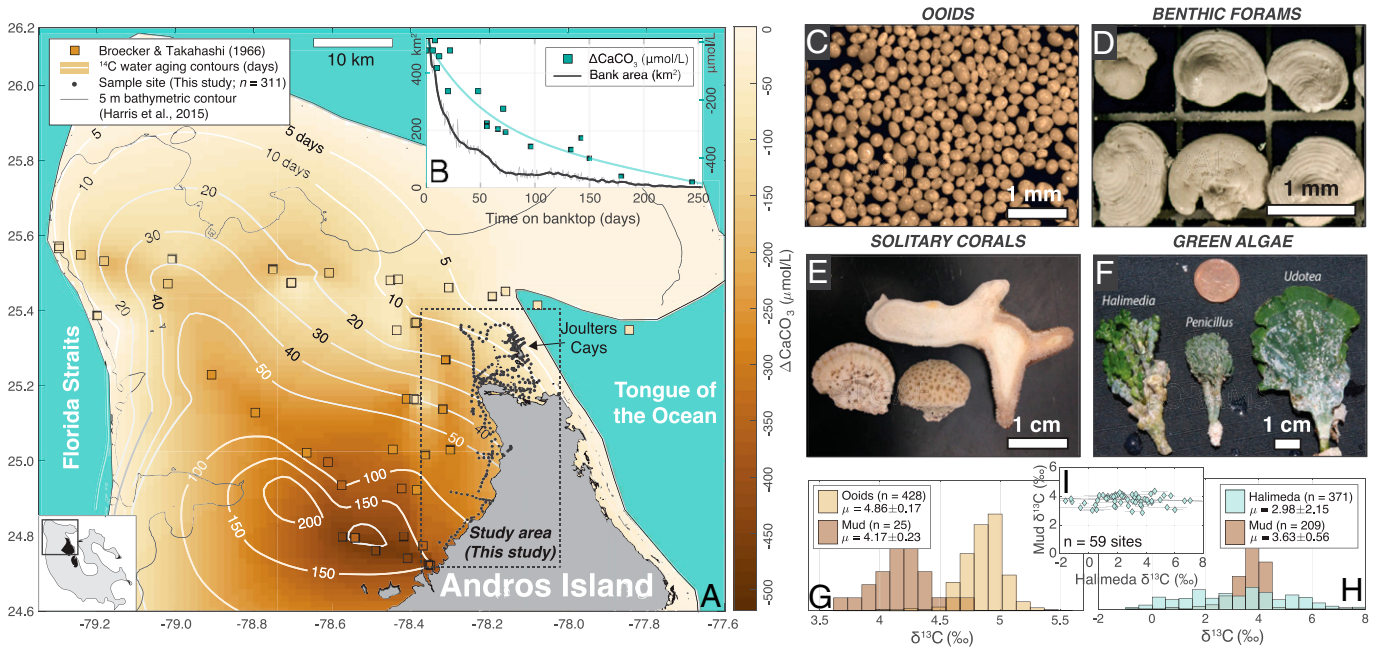

Fig. 1. Carbonate production on the GBB, which is mostly shallower than 5 m [Harris et al. (17)]. (*A* and *B*) Seawater ^{14}C, pCO_2, and alkalinity data from Broecker and Takahashi (30) illustrate a pattern of progressive carbonate precipitation ($\Delta CaCO_3$) from aging banktop waters. Based on the data in *A* and *B*, an estimated 91% of all precipitated carbonate has formed from waters before the 50-day contour, and 64% has formed before the 10-day contour. (*C*–*F*) Significant carbonate constituents on the GBB include ooids (*C*), foraminifera (*D*), solitary corals (*E*), and green algae (*F*). The abrasion or disintegration of any of these carbonate constituents (*C*–*F*) could contribute to the carbonate mud observed across the bank. (*G*–*I*) $\delta^{13}C$ data cast doubt on the hypotheses that carbonate mud is sourced primarily from ooids (9) or green algae (7, 20, 25). (*G*) Co-occurring ooids and mud (<63 μm) represent two distinct and nonoverlapping $\delta^{13}C$ populations. (*H* and *I*) Although the $\delta^{13}C$ values of *Halimeda* (algae) and mud are overlapping (*H*), there is zero correlation between the $\delta^{13}C$ of *Halimeda* and that of co-occurring mud at a series of 59 stations from Joulters Cays to west Andros (*I*). In other words, $\delta^{13}C_{mud}$ does not track $\delta^{13}C_{Halimeda}$. The error bars in *I* represent the 1σ of $\delta^{13}C$ values in the 2 to 50 grains of *Halimeda* carbonate measured at each site.

exported from platforms that lack documented whiting events (33). In regard to the algal precipitation hypothesis (7, 20, 25), carbonate Sr concentration data have been used to argue that green algae cannot be the dominant source of Bahamian mud, since algal aragonite has lower Sr concentrations than bulk muds (36). Also, if modern carbonate mud were sourced primarily from the breakdown of algae (7, 20) or skeletal grains (26–29), one would need to invoke additional mechanisms for mud formation to explain the thick sequences of carbonate mudstone that exist prior to the evolution of carbonate biomineralizing organisms (1). Ooid abrasion (9) offers a convenient mechanism that could operate throughout Earth history, yet $\delta^{13}C$ observations (10) show that carbonate mud and ooids represent distinct and nonoverlapping geochemical populations (Fig. 1*G*), challenging the notion that mud is derived primarily from ooids.

It is likely that all of the aforementioned processes—water-column precipitation, algal disintegration, and grain abrasion—produce at least some mud-sized sediment. Recent work by Gischler et al. (29) demonstrated that carbonate mud in some locales is dominated by skeletal microfragments, and, in other locales—most notably the Bahama Banks—appears to be largely nonskeletal. Here, we seek to understand the systematics of this nonskeletal mud production: When, where, and how does mud form, and does nonskeletal mud production require specific seawater geochemistry?

Field Site

We focus on the region northwest of Andros Island on the GBB (Fig. 1*A*). This region has a rich history of geological investigation (15, 16, 21) and has remained at the forefront of the carbonate mud debate (8, 22–24, 30, 32). Also, the observations of Broecker and Takahashi (30) in this region, which include ^{14}C-based banktop water ages [utilizing the bomb spike (30, 31)], enable the quantification of carbonate precipitation in both space and time (Fig. 1 *A* and *B*), providing rare constraints for numerical models of carbonate formation.

Sampling and Geochemical Analyses

The predominant carbonate constituents on the GBB that are larger than the mud fraction include ooids and coated grains, benthic foraminifera, solitary corals, and green algae (Fig. 1 *C*–*F*). We sampled all carbonate constituents across a transect that links the high-energy ooid shoal environments near the platform margin to the muddy western shores of Andros Island, near some of the oldest and most sluggishly mixed platform waters (Fig. 1*A*) (30). To characterize carbonate mud, we sampled bulk sediment and sieved the <63-μm size fraction. Samples were analyzed for $\delta^{13}C$ and $\delta^{18}O$ on a Sercon continuous-flow isotope ratio mass spectrometer ($n = 2,007$; *SI Appendix*, Fig. S3) (10) and for major-, minor-, and trace-element concentrations (Ca, Mg, Sr, Li, and U; $n = 247$) on a Thermo Fisher I-Cap Q inductively coupled plasma mass spectrometer (ICP-MS). A subset of mud ($n = 12$) and ooid ($n = 2$) samples were measured for clumped isotope compositions (Δ_{47}) in order to constrain the carbonate formation temperature (37) and aid in distinguishing between different mud-formation hypotheses.

Results and Discussion

Using Geochemical Fingerprints to Constrain the Source of Mud. We evaluate the hypothesis that mud is sourced primarily from the abrasion/breakdown of ooids (9) or algae (7, 20). We begin by considering the $\delta^{13}C$ observations. We find that the $\delta^{13}C$ compositions of ooids (4.86 ± 0.17‰) and mud

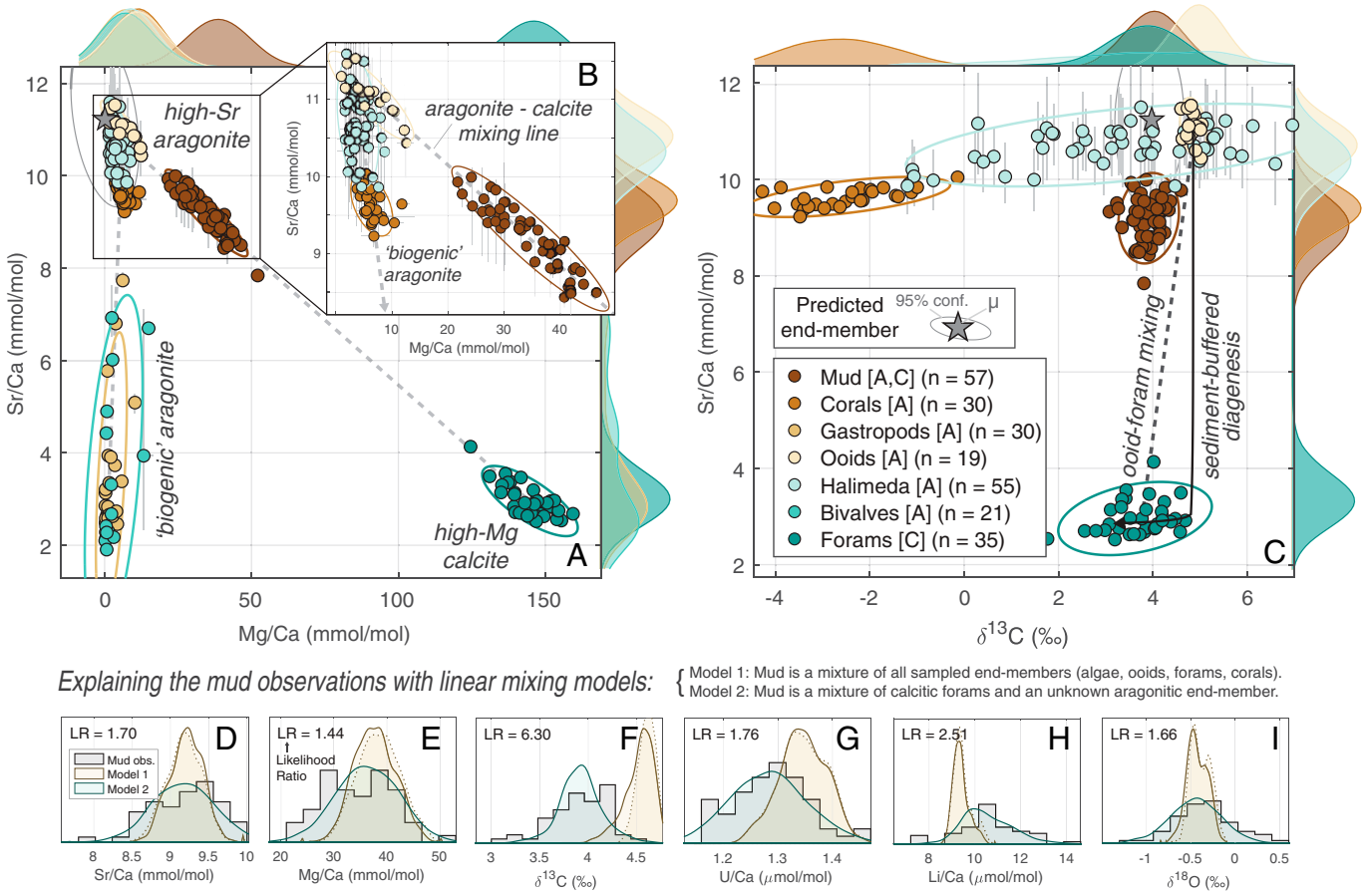

Fig. 2. Geochemical fingerprinting of carbonate mud. (*A–C*) Crossplots of Mg/Ca, Sr/Ca, and δ^{13}C compositions of the mud fraction (<63 μm) and dominant carbonate constituents on the GBB, including corals, gastropods, ooids, *Halimeda* algae, bivalves, and foraminifera (Fig. 1 *C–F*). The brackets in the legend in *C* denote whether each constituent is aragonite [A] or calcite [C]. Note that the Mg–Sr data (*A*) demonstrate that gastropods and bivalves cannot be important constituents of mud, so these categories are excluded from the plot in *C* to reduce clutter. (*D–I*) Results of linear mixing models aimed to represent mud as a mixture of abraded end-members. The gray histograms depict the measured compositions of the $n = 57$ mud samples, while the beige and green distributions represent the predicted mud compositions based on mixing models constrained by the data in *A–C*, as well as the other geochemical data (U/Ca, Li/Ca, and δ^{18}O; *SI Appendix*, Fig. S4). Model 1 tries to explain mud as a mixture of all probable mixing end-members (algae, ooids, foraminifera, and corals). The optimum mix of end-members in Model 1 is ~77% ooids, ~22% forams, ~0% corals, and ~0% Halimeda. In other words, algae and corals are unlikely to contribute significantly to the observed (obs.) mud. To illustrate this point, we implement a variation of Model 1, in which ooids and forams are the only end-members; the results of this model—shown with dashed brown lines in *D–I*—are nearly identical to those of Model 1. Model 2 explains mud as a mixture between foraminifera (calcite) and an unknown (not directly sampled) aragonitic end-member. The model predicts mud averaging 77.1% aragonite, which agrees with our prediction based on the spread of mud values along the Mg vs. Sr mixing line in *A* (78.1 ± 5.0% aragonite) and is independently verified by $n = 6$ XRD measurements (78.5 ± 6.0% aragonite, 21.5 ± 6.0% high-Mg calcite). The predicted geochemical composition of the aragonitic end-member is depicted by the gray stars and gray 95% confidence (conf.) ellipses in *A* and *C*. L.R. describes the likelihood ratio of Model 2 vs. Model 1. For example, the L.R. value of 6.30 in *F* means that, based just on δ^{13}C data, Model 2 is ~6× more likely to explain the observations than Model 1. When the likelihood ratios in *D–I* are taken together in a full multivariate model, Model 2 is an estimated 98× more likely than Model 1.

(4.17 ± 0.23‰) are distinct and nonoverlapping (Fig. 1*G*). Likewise, although the mean δ^{13}C of algae (2.98 ± 2.15‰) is within uncertainty of the mean mud value (Fig. 1*H*), a comparison of $n = 59$ sites where both mud and *Halimeda* algae are present yields no correlation between the δ^{13}C values of algae and mud (Fig. 1*I*). Thus, based on δ^{13}C alone, we propose that mud is not dominantly sourced from the singular breakdown of co-occurring ooids or algae. However, mud can be derived from multiple sources and then mixed, homogenized, and transported (26, 29). As a result, mud need not carry the identical δ^{13}C signature as its parent sources. We use measurements of a suite of geochemical parameters—including minor and trace elements, δ^{13}C, and δ^{18}O—to evaluate whether mud can be described as a mixture of all major banktop carbonate sources (10): ooids (9), algae (7, 20), foraminifera (26), corals, bivalves, and gastropods (Fig. 2).

Fig. 2*A* illustrates how mineralogy controls the Mg and Sr composition of the various carbonate constituents. The population of mud samples ($n = 57$) falls along a mixing line between a high-Sr source of aragonite and high-Mg calcite (Fig. 2*A*). Based only on the correlation between Sr and Mg depicted in Fig. 2*A*, describing mud as the abraded mixture of ~80% ooids (aragonite) and ~20% foraminifera (high-Mg calcite) would represent an excellent fit to the data. However, as we consider other geochemical parameters besides Mg and Sr, this ooid–foraminifera mixing model falls apart. In particular, the δ^{13}C value of mud is ~0.8‰ too low to be explained by the mixing of ooids and foraminifera (Fig. 2*C*). Both δ^{13}C and Sr/Ca can be altered through meteoric and marine diagenesis (38), but a simple diagenetic model (38, 39) predicts [Sr] to be altered before δ^{13}C (38, 39), which is opposite to the pattern observed in our dataset (Fig. 2*C*).

To summarize, a two-component (ooid–foraminifera) mixing model is insufficient to explain the geochemical composition of mud, so we ask whether incorporating small quantities of additional end-members, such as *Halimeda*, corals, bivalves, and gastropods, can solve the problem. For example, corals have such low δ^{13}C (10, 12) that only a small (<15%) addition of coral-derived aragonite could draw down the δ^{13}C of mud by

the requisite ∼0.8‰. However, corals also have $\delta^{18}O$ values so low that such a mixture would shift the mud $\delta^{18}O$ population by ∼0.5‰, outside of the range observed (Fig. 2*I*). We perform a systematic survey to evaluate whether any mixture of the six macroscopic constituents in Fig. 2 can explain the geochemical population of carbonate mud. We use bootstrap resampling to formulate probabilistic mixing models in which we solve for the combination of end-members that can best reproduce the joint distributions of Sr/Ca, Mg/Ca, Li/Ca, U/Ca, $\delta^{13}C$, and $\delta^{18}O$ of mud (Fig. 2 and *SI Appendix*, Fig. S4). We find that, despite the large number of degrees of freedom, even the best-fitting models significantly overestimate the $\delta^{13}C$ and U/Ca and underestimate the Li/Ca compositions of mud (Fig. 2 *D–I*, Model 1). We interpret the inability of this mixing model to reproduce the observed geochemical signature of mud to indicate the presence of an additional, geochemically distinct source of carbonate.

The correlation between Mg/Ca and Sr/Ca for the mud samples indicates that the mud is composed of high-Sr aragonite and high-Mg calcite (Fig. 2*A*). As such, we propose that the "missing" carbonate source must be one of these two end-members. The only abundant source of calcite on the banktop, based on macroscopic and microscopic (scanning electron microscopy [SEM]) observations of the sediments (*SI Appendix*, Fig. S2), is foraminiferal calcite (10, 26, 29, 36, 40). In contrast, even some of the earliest SEM observations of Bahamian mud (36, 40) led workers to conclude that there must be a source of aragonite needles that is distinct from algae or grain abrasion (29, 36, 40). We have a chance to use the geochemical fingerprints in Fig. 2 to predict and explain the identity and chemistry of this missing carbonate source.

We first formulate the inverse problem, in which we seek to describe carbonate mud as a mixture of forams and an unobserved aragonite end-member. Using Markov Chain Monte Carlo (MCMC) methods, we generate probabilistic estimates for the aragonite end-member composition (Fig. 2 *A–C*). This two-component mixing model, whereby mud is 77.1% sourced from the aragonite end-member and 22.9% sourced from the calcitic foram end-member, can fully reproduce the observed geochemical distributions of our mud samples (Fig. 2 *D–I*). Overall, this two-component model is an estimated 98× more likely to explain the geochemical data in Fig. 2 *D–I* than the model based on the mixing of all probable end-members (algae, ooids, forams, and corals).

For completeness, we also consider the scenario in which carbonate mud is a mixture of the ooids (high-Sr aragonite) and an unobserved high-Mg calcite end-member, since, theoretically, high-Mg calcite could be produced by some coccolithophores (41), red algae (26), and even inorganic precipitation (42, 43), albeit at very slow growth rates (43). Formulating an MCMC model as above, the observed population of mud samples would require a calcitic end-member with $\delta^{13}C$ ranging from 0.3‰ to −3.0‰ to −12.9‰ in the scenarios in which the high-Mg calcite is 0%, 50%, and 80% foraminifera, respectively (with the remaining high-Mg calcite sourced from the "unobserved" end-member). This $\delta^{13}C$ value is 1 to 14‰ lower than predicted for precipitation from all measured Bahamian waters (44), including porewaters depleted in $\delta^{13}C$ through remineralization of organic carbon (45).

Thus, after evaluating all mixing possibilities, the most parsimonious is a system dominated by two components: foraminiferal calcite [both the most abundant and the least robust bioclast observed on the banktop (10)] and a nonskeletal, high-Sr aragonite.

Differentiating between Mechanisms of Mud Formation. Our geochemical fingerprinting builds on previous textural and geochemical observations (26, 29, 36, 40) and supports the existence of an additional source of aragonite that is geochemically distinct from all sampled macroscopic end-members (Fig. 2). We posit that this source represents a direct precipitate. There are two modes of mud production that could fit the direct-precipitation hypothesis:

1. Banktop whiting events (22, 24, 32): The whiting mechanism implies that mud formation does not occur uniformly across space or time, but, rather, is restricted to a narrow region west of Andros Island (24, 32) that hosts sporadic whiting events (Fig. 3*B*). During whitings, the water adopts a milky white appearance because it is filled with ∼10 mg/L suspended fine-grained carbonate (compared to 1.5 mg/L typical of "clear" banktop waters) (22). However, there is no consensus about whether the suspended particles represent new precipitation (22, 24), the resuspension of mud-sized sediment from the seafloor (31), or a combination of the two (47).
2. Progressive precipitation from supersaturated waters (21, 30, 47): Even the earliest observations of carbonate chemistry on the Bahama Banks (8, 21, 30) revealed a clear pattern of alkalinity depletion from shelf edge to bank interior (Fig. 1*B*), reflecting continued carbonate precipitation in aging banktop waters. Cloud et al. (21) referred to this process as "the progressive chemical equilibration of a disequilibrium state." Broecker et al. (48) likened the parcels of water traversing the banktop to boxcars on a slow-moving cargo train, unloading precipitated carbonate along the journey until the waters became too depleted in alkalinity to produce more carbonate (30, 47). Previously, it has been assumed that carbonate forms only on the banktop (36, 49). However, the water mass surrounding the Bahama Banks has remarkably high Ω_A throughout the upper few hundred meters of the water column (see Fig. 7*B*). For example, despite the cold temperatures and high pressures, seawater down to ≥600 m on the flanks of the Bahama Banks has Ω_A higher than in the sluggishly mixed <1-m-deep waters along the western margin of Andros Island (see Figs. 4*A* and 7*B*). These observations open up the possibility that nonnegligible carbonate formation could occur in deeper, alkaline waters on the bank margins and upper periplatformal slopes (50). In other words, Broecker's cargo train begins unloading its boxcars before parcels of ocean water reach the platform.
   More specifically, consider the trajectory of a parcel of water on the eastern margin of the Bahama Banks. As the water is pushed onto the shallow banktop by prevailing easterly winds, the water warms, depressurizes, and releases CO_2 to the atmosphere, elevating the aragonite saturation state (Ω_A) and favoring precipitation (51). In the bank interior, alkalinity-depleted water masses support less and less carbonate production (Fig. 1), like the desert behind a coastal mountain range that has wrung the moisture out of a parcel of air. The initial alkalinity of the water mass sets the threshold for how much carbonate can be precipitated; just as wet air masses generate more rain, alkaline water parcels support more productive carbonate factories. Finally, carbonate precipitation depends not only on favorable seawater chemistry, but also on the availability of condensation nuclei. Fine carbonate particles, easily suspended by waves and currents, provide excellent substrates for carbonate precipitation as epitaxial growth (47).

To differentiate between these two mechanisms—1) spontaneous whiting events vs. 2) progressive precipitation—we return

to the geochemical signature of carbonate mud. We employ clumped-isotope thermometry, which uses the abundance of carbonate groups with two rare isotopes (dominantly ^{13}C–^{18}O) compared to a random distribution of isotopes among all isotopologues (Δ_{47}), to derive the seawater temperature at the time of carbonate formation (37). Clumped isotopes are a useful tool here because the two hypotheses make different predictions about the formation temperature of carbonate mud (Fig. 3).

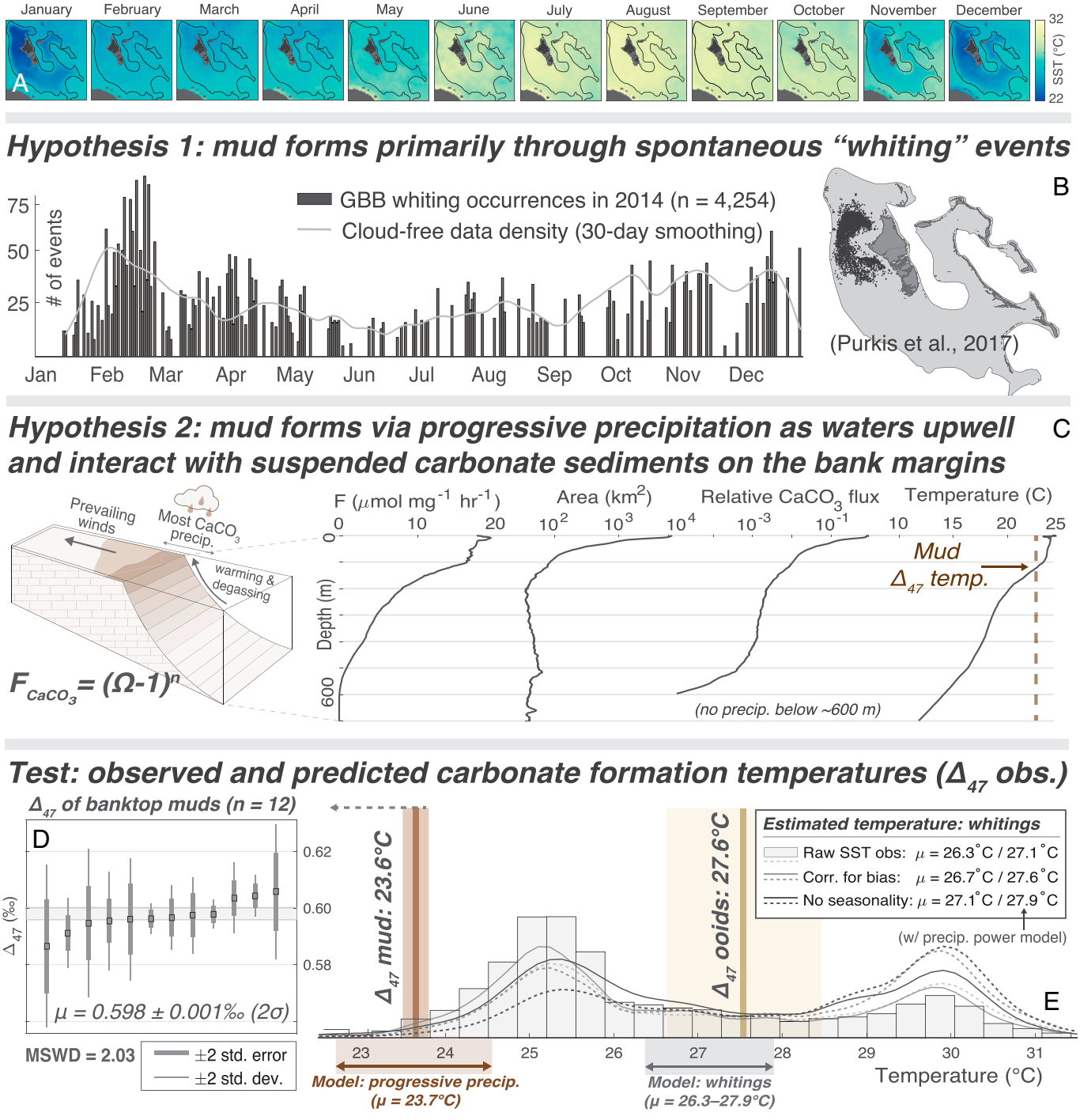

Fig. 3. Temperature observations constraining the locus of mud formation. (*A*) Sea-surface temperature data based on MODIS observations from 2014 show that banktop temperatures range from 22 to 32 °C. (*B*–*E*) We estimate the formation temperatures of carbonate mud produced in two scenarios and compare the predictions to clumped-isotope (Δ_{47}) observations. (*B*) First, to estimate the average temperature of whiting-derived carbonate, we sample the daily sea-surface-temperature datasets (*A*) at the spatiotemporal locations of $n = 4,254$ whiting occurrences documented from 2014 [Purkis et al. (32)]. (*C*) Second, we consider a model in which mud forms across the banktop, bank margins, and upper slopes at a rate (52) proportional to $(\Omega_A - 1)^n$. The predicted average temperature of precipitated carbonate (integrated across all depths, although note that the majority of production occurs at depths <20 m) is $\mu = 23.7$ °C. (*D*) The Δ_{47} values of banktop mud samples all are virtually the same, consistent with the hypothesis that these samples represent a single Δ_{47} population. The mean Δ_{47} of the population in *D* is 0.598, which corresponds to a carbonate formation temperature of 23.6 °C (54). (*E*) The mean Δ_{47} observations of mud are consistent with predictions for the "progressive precipitation" model (*C*), but ~3.5 °C lower than the predicted temperature for the whitings scenario (*B*). The left-pointing gray arrow from the bulk mud Δ_{47} temperature (23.6 ± 0.3 °C) illustrates that accounting for mud's ~20% contribution of foraminiferal calcite (which should record warmer temperatures more similar to the mean banktop water temperature (~27 °C) (10) pushes the aragonite-formation temperature to even lower values (~22.8 °C). The Δ_{47}-based temperatures for ooids (27.6 ± 0.9 °C; $n = 2$) are warmer than those of mud and are consistent with the predictions based on annual patterns of sea-surface temperatures within the ooid belt (*A*) (21, 55). Corr., corrected; dev., deviation; obs., observations; precip., precipitation; std. standard.

We model the predicted temperature under each scenario, and compare the results to Δ_{47} observations from banktop mud samples.

Banktop whitings. To model the temperature of mud formed during whiting events, we sample satellite-derived sea-surface-temperature estimates (Fig. 3*A*) at the location and time of each of 4,254 whiting events identified (32) in satellite imagery (Fig. 3*C*). We find that the average seawater temperature during whitings is 26.3 to 27.1 °C. Next, we account for the fact that the precipitation "power" of a parcel of cool ocean water delivered onto the bank [through the spalling of currents from the Florida Straits—the most recently proposed mechanism for whiting events (32)] varies through the year. For example, if a 20 °C parcel of water spills onto the bank (32) in the summer, its temperature may rise by 10 °C (Fig. 3*A*). This temperature change, and the resulting CO_2 evasion, serves to elevate Ω_A by 0.25 and increase the carbonate precipitation flux by a factor of 5.7 (*SI Appendix*, Fig. S5). Using a box model to track carbonate system parameters and the resulting carbonate precipitation flux (*SI Appendix*, Fig. S8), we weight each whiting observation in Fig. 3*C* by the relative amount of carbonate precipitated from that event and obtain a temperature distribution of whiting-derived carbonate that is elevated by ∼1 °C compared to the unweighted sampling of the satellite data (*SI Appendix*, Fig. S7). Finally, notice that there is an apparent seasonality of whitings in the published record (32), whereby events are most common in the winter and early spring (Fig. 3*B*). However, this apparent seasonality correlates with the relative abundance of cloud-free satellite imagery used to detect the whitings (Fig. 3*B*), highlighting the possibility of an observational bias. Therefore, as an additional treatment of the data in Fig. 3*B*, we compute the predicted temperature distribution after normalizing the whiting record by the abundance of cloud-free imagery. All told, these varied treatments of the whitings dataset (32) produce temperature predictions ranging from 26.3 to 27.9 °C ($\mu = 27.1$ °C) (Fig. 3*D*).

Progressive precipitation from supersaturated waters. We consider the simple model in which the carbonate precipitation flux (F_{CaCO_3}) is a function of saturation state (47, 52, 56):

$$F_{CaCO_3} = (\Omega_A - 1)^n. \quad [1]$$

We apply this equation, experimentally calibrated for Bahama Bank sediments (Fig. 4*B*; ref. 47), to spatial maps of Ω_A, pressure, and temperature across the Bahamaian archipelago. On the banktop, we calculate Ω_A using the chemical observations of Broecker and Takahashi (30) (Fig. 4*A*) and estimate sea-surface temperatures using daily Moderate Resolution Imaging Spectroradiometer (MODIS) Terra thermal infrared data (Fig. 3*A*). In the deeper waters surrounding the Bahama Banks, we apply the depth-dependent temperature and Ω_A profiles from oceanographic bottle data (see Fig. 7*B*) to the hypsometry of the Bahamas region (Fig. 3*C*). We find that the majority of precipitation occurs in waters ≤20 m, but that precipitation can occur at depths up to ∼600 m (Fig. 3*C*). All told, the predicted Bahamas-wide Δ_{47} formation temperature of carbonate mud is $\mu = 23.7$ °C (Fig. 3*D*). Note that this result integrates precipitation at all depths. While shallow carbonate production can be exported to deeper waters (36, 49), the reverse scenario is less well known. In other words, we are not proposing that carbonate produced at 500-m water depth finds its way onto the banktop. We can compute the formation temperature of banktop muds by integrating the depth-dependent production (Fig. 3*C*) across only the upper 30 m of the water column, for example, and estimate a formation temperature of $\mu = 23.9$ °C.

Evaluating the Evidence: Where Is Carbonate Mud Produced? Armed with predictions for the carbonate formation temperatures under the whiting and progressive precipitation scenarios (Fig. 3 *B* and *C*), we are ready to examine the Δ_{47} observations of banktop muds. A striking feature of our Δ_{47} dataset is the lack of variability between samples. Of the 45 individual analyses of $n = 12$ mud samples spanning the study area ($n \approx 4$ replicate analyses per sample), the SD for the Δ_{47} is 0.009‰, which is comparable to instrument precision. In other words, the Δ_{47} observations are consistent with the hypothesis that these samples represent a single population. To quantify this concept another way, we compute the mean squared weighted deviation (MSWD) (a metric frequently used in geochronology to assess the heterogeneity of a population relative to the uncertainties of the analytical measurements; ref. 53), and obtain a value of 2.03 (Fig. 3*D*), which also is consistent with the inference that these Δ_{47} observations represent a single population (53). The formation temperature inferred from this population is 23.6 ± 0.3 °C ($\mu \pm 1\sigma$) (Fig. 3*D*) (54).

Note that this mean temperature of 23.6 °C falls below the 5th percentile of the temperature distribution for whiting-derived carbonates (Fig. 3*D*). In other words, the clumped isotope thermometry suggests that banktop muds are too cold to have been formed during whiting events. However, we acknowledge that the ∼3.5 °C difference between our Δ_{47} observations and the predictions for whitings is relatively small. Therefore, we treat the clumped isotope observations as consistent with—but not necessarily proof of—the inference that whitings are not responsible for the majority of Bahamian mud. We turn to other geochemical and sedimentary evidence to test this hypothesis.

1. Seawater saturation state: Satellite observations have shown that whitings are not randomly distributed across the Bahama Banks, but rather clustered in a particular region west of Andros Island (24, 32) (Fig. 3*C*). We note that this whiting zone is, from the perspective of seawater geochemistry, one of the least favorable places to precipitate carbonate (Fig. 4). For example, based on laboratory experiments of carbonate precipitation kinetics in Bahamian seawater (47), an average parcel of water in the whiting zone would support a carbonate precipitation flux ∼4 times lower than a parcel of water near the bank edge (Fig. 4*C*). These observations do not preclude that whitings could be a source of carbonate. However, a conclusion from Fig. 4 is that, if there is direct precipitation of carbonate mud within the whiting zone, there should be significantly more (≥10×) carbonate production outside the whiting zone—an argument articulated by Morse et al. (47). Also, while the availability of condensation nuclei almost certainly plays a role in mud production, an estimated >98% of fine-grained suspended carbonate resides outside the visually dramatic whiting zone (47).
2. Sedimentary records from the periplatform: For over 50 years, it has been known that there are thick accumulations of nonskeletal aragonite mud in the deep waters surrounding Bahama Banks (33, 34, 36, 49) (Fig. 5). These muds have been assumed to represent export from the platform (33, 36, 49). The spatial and temporal records of these deep-water sedimentary deposits present two challenges to the whiting hypothesis. First, from the spatial perspective, there is significant mud accumulation in basins with no connectivity to documented whiting regions (e.g., cores 5 and 6 in Fig. 5). Second, from the temporal perspective, sediment cores reveal thick accumulations of pristine aragonite mud (34, 36) dated to the last glacial period (33, 34) (Fig. 5*C*). If mud formed

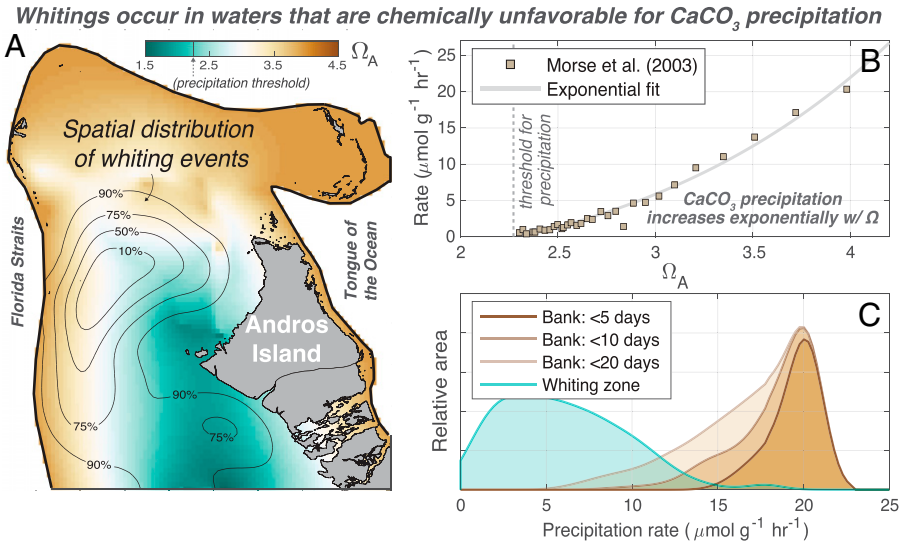

Fig. 4. An exploration of carbonate saturation state and precipitation kinetics in the whiting zone. (*A*) Aragonite saturation state, based on the water chemistry data from Broecker and Takahashi (30), and whiting occurrence data (32). The 90% contour encapsulates 90% of documented whitings. (*B*) Carbonate precipitation kinetics based on experiments with Bahama Bank sediment [Morse et al. (47)]. (*C*) Estimated precipitation rates for different regions of the banktop based on the spatial distribution of Ω_A (*A*) and the experimental kinetics data in *B*. Note that waters along the bank margins—represented here as the regions with banktop water ages less than 5, 10, and 20 days—support precipitation rates that are 3 to 4× larger than waters within the whiting zone.

primarily through banktop whitings (22, 24), mud production should shut off during glacial periods, since the shallow Bahama Banks were subaerially exposed.

A Model for Carbonate Mud Formation on the Bahama Banks. The scenario that can simultaneously explain mud's spatiotemporal distribution (Fig. 5) and geochemical fingerprint (Figs. 2 and 3) is the hypothesis of widespread, progressive mud production from the bank margins and across the banktop (21, 30, 47, 48). Under this hypothesis, peak mud production occurs on the platform rims (Fig. 6*A*), where upwelled parcels of water have warmed, depressurized, and degassed CO_2 (all of which cause Ω_A to rise) (51). A less productive mud factory exists on either side of the platform rim (Fig. 6*A*). In the bank interior, carbonate precipitation leaves the sluggishly mixed banktop waters depleted in alkalinity, so precipitation rates decline with increasing water age (Fig. 1*B*). This region is akin to the desert downwind of a mountain range. Likewise, in the deeper waters on the platform slopes, cold temperatures and high pressures combine with carbonate's retrograde solubility to disfavor mineral precipitation (51).

It is likely that the mud factory requires not only favorable seawater chemistry, but also the presence of condensation nuclei and/or a mineral substrate onto which the carbonate can precipitate (47, 57). This requirement of available mineral surface area (47) may explain why the waters that source the Bahama Banks (Fig. 7) do not precipitate carbonate in the middle of the Atlantic Ocean. The topographic rise on the margins of the Bahama Banks puts supersaturated waters in contact with fine-grained carbonate sediment, which, through normal wave action and currents, fills

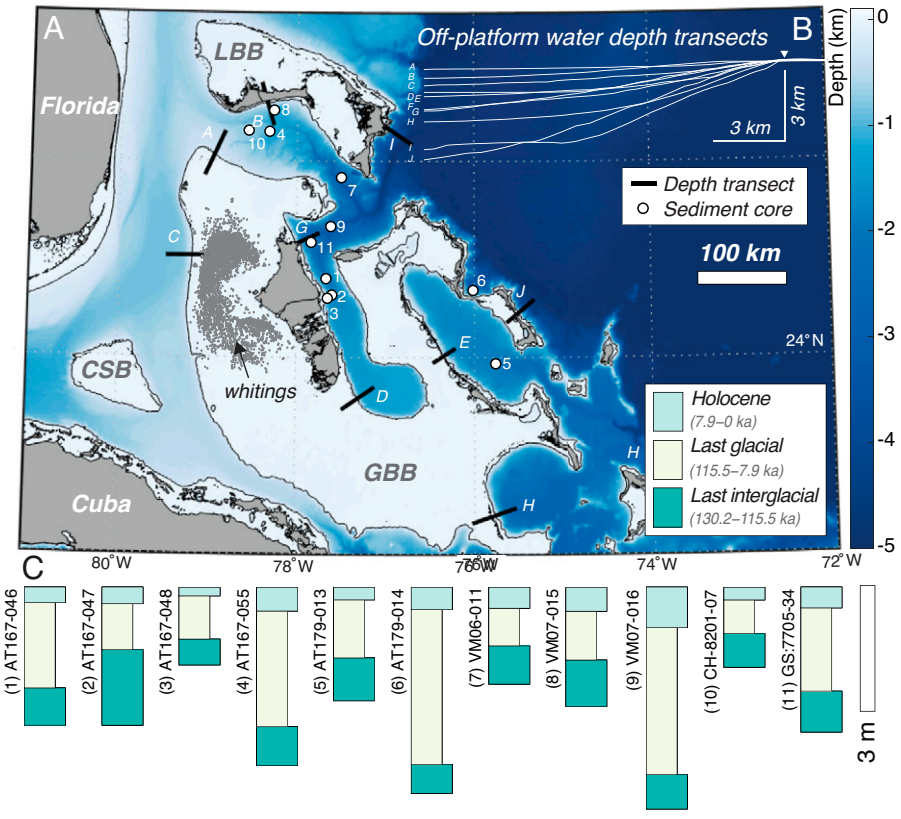

Fig. 5. A case for widespread carbonate mud precipitation on the margins of the Bahama Banks. (*A* and *B*) Geography of the Bahamas. Water-depth transects are labeled with capital letters, sediment cores are labeled with numbers, and whitings (32) are depicted with gray dots. CSB, Cay Sal Bank; LBB, Little Bahama Bank. (*C*) Shallow sediment cores from the periplatformal slopes and proximal basins constrain sediment accumulation during the Holocene, last glacial, and last interglacial periods (33). Note that there is significant carbonate accumulation [including nonskeletal aragonite mud that cannot be attributed to pelagic sources (33)] during the last glacial period, when the Bahamian platforms were subaerially exposed. Thus, aragonite mud production persists during glacial lowstands. Also, thick sequences of aragonite mud have accumulated on periplatform locations with no connectivity to the whiting zone.

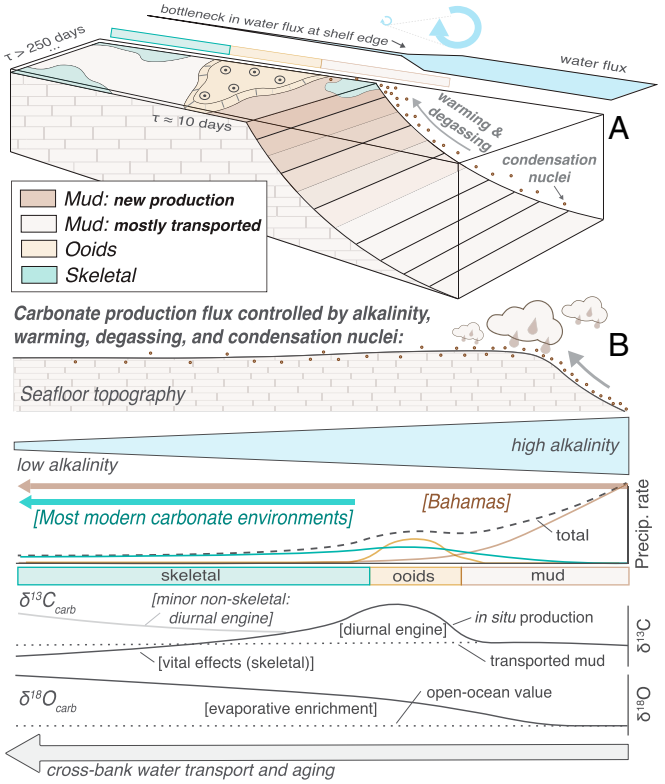

Fig. 6. A model for carbonate production on the Bahama Banks. (*A* and *B*) Highly alkaline waters from the west Atlantic (Fig. 7) reach the bank margins, where they warm, degas CO_2, interact with condensation nuclei (i.e., fine carbonate particles), and precipitate carbonate. This precipitation leaves the residual waters depleted in alkalinity. The ooid belt occurs at the intersection of the still chemically favorable waters with the shallow, wave-agitated zone. In this region, the water mass is sufficiently shallow and restricted to support a diurnal carbon engine (13), whereby Ω_A is elevated each day during the hours of peak photosynthesis, enabling nonskeletal carbonate precipitation (with an elevated $\delta^{13}C$ signature; Fig. 1*G*) to occur, even if the time-averaged seawater chemistry has lower Ω_A than at the bank margin. Calcifying organisms (e.g., foraminifera, corals, and green algae) can produce carbonate in all regions of the photic zone and likely account for much of the production in the bank interior. In this way, the alkalinity of the source waters dictates what types of carbonate can be precipitated: 1) The nonskeletal mud factory requires the highest alkalinity. 2) The ooid factory can sustain precipitation from less alkaline waters because of the diurnal carbon engine. 3) Skeletal production can persist in the least chemically favorable waters, thanks to the carbonate-concentrating mechanisms employed by calcifying organisms (12). Most modern carbonate factories operate only in this realm of skeletal production.

even optically clear waters with relatively high concentrations of suspended carbonate (~1.5 mg/L) (22, 47).

Finally, this progressive precipitation model (Fig. 6*A*) makes a series of predictions regarding the stable isotope signature of carbonate formed at different parts of the Bahama Banks (Fig. 6*B*). For example, nonskeletal carbonate formed on the bank margins and upper slopes should have relatively "normal" $\delta^{13}C$, reflective of the dissolved inorganic carbon (DIC) of the oceanic source waters. [Note that the equilibrium fractionation factor from HCO_3^- to aragonite (46) is +2.7‰, so seawater with $\delta^{13}C_{DIC} \approx 1.3$‰ produces aragonite with $\delta^{13}C \approx 4$‰.] In contrast, nonskeletal carbonate formed in the bank interior (where Ω_A is lower) will rely on a diurnal carbon engine (13) to elevate Ω_A and favor precipitation. In this case, the mechanism that elevates Ω_A (transferring more of the water's DIC into organic matter during the hours of peak photosynthesis) involves a concomitant increase in the $\delta^{13}C$ of DIC and, thus, the $\delta^{13}C$ of precipitated carbonate (13). Indeed, $\delta^{13}C$ observations of mud from the bank interior (44) display elevated $\delta^{13}C$ values compared to the dataset concentrated closer to the bank margin (10) (*SI Appendix*, Fig. S22). These isotopic data (44) are consistent with the presence of some in situ precipitates toward the bank interior, which could either represent a small amount of whiting-derived carbonate (22) or simply the $\delta^{13}C$-enriched carbonate squeezed out of the most alkalinity-depleted waters. The work of Gischler et al. (29) offers additional isotopic evidence for progressive precipitation across the banktop. These workers separated Bahamian muds into three size fractions and found that, while the mineralogy remained relatively constant (97.2%, 94.5%, and 94.2% aragonite for the <4-μm, 4- to 20-μm, and 20- to 63-μm sizes, respectively), the $\delta^{13}C$ steadily increased from the smallest to the largest particles (2.54‰, 3.30‰, and 4.38‰). This implies that, as carbonate particles get larger and larger—and are transported predominantly in the direction from the shelf edge to the bank interior—the new carbonate forming as epitaxial growth caries a more and more enriched $\delta^{13}C$ signature.

For carbonate $\delta^{18}O$, we expect nonskeletal material formed near the bank margin to carry a $\delta^{18}O$ signature similar to that of the oceanic source waters, whereas carbonate formed in the bank interior should have elevated $\delta^{18}O$ due to the evaporative enrichment of aging banktop waters (*SI Appendix*, Fig. S16). The mud samples in our dataset have $\delta^{18}O$, consistent with bank-margin waters (10), and mud samples collected in the bank interior (44) show elevated $\delta^{18}O$, consistent with continued precipitation across the evaporative enrichment trajectory (*SI Appendix*, Fig. S22).

Lastly, the paired Δ_{47}–$\delta^{18}O$ observations offer an additional constraint on the locus of carbonate formation. We consider the Δ_{47} and $\delta^{18}O$ values of mud vs. ooids. Although mud and ooids have almost identical $\delta^{18}O_{carb}$ values (-0.25 ± 0.36‰ and -0.13 ± 0.23‰, respectively; *SI Appendix*, Fig. S3), the Δ_{47} observations suggest that ooids form in waters that are ~4.0 °C warmer (Fig. 3*E*), a temperature difference that should act to decrease $\delta^{18}O_{carb}$ by ~0.8‰ (*SI Appendix*, Fig. S19). Thus, we can infer that ooids form in waters that have been enriched in $\delta^{18}O_{water}$ by ~0.8‰ relative to the waters in which muds form. In other words, the ooid belt, which is located in shallow waters near the platform rim (17, 55), represents a region that is evaporatively enriched relative to the predominant mud production zone in the less-restricted waters of the platform margin (Fig. 6).

Why Is Nonskeletal Mud Rare in the Modern Ocean? A Link to the "Oolite Problem". Any model for carbonate mud formation must also explain why the occurrence of nonskeletal mud on Earth today is rare and spatially nonrandom. In particular, there are only two documented instances of significant nonskeletal mud formation in the modern ocean, and both are located in the west Atlantic (29). Workers have considered a similar enigma (59, 60) of why virtually all (94%) of the occurrences of modern ooids forming in normal marine conditions are in the west Atlantic. Of those ooid occurrences, the majority are on the Bahama Banks (*SI Appendix*, Fig. S23). Are there unique physical, chemical, or biological conditions that are achieved in the Bahamas, but not elsewhere (61)? We examine a range of physical and chemical parameters from shallow carbonate locales around the world, including the concentration of phosphate [a kinetic inhibitor for $CaCO_3$ precipitation (57)], aragonite saturation state, sea-surface temperature, salinity, wind speed, and chlorophyll-A (*SI Appendix*, Figs. S23–S25). The only parameter for which the Bahamas are virtually unique in the world is alkalinity (Fig. 7*D*).

The inference that high alkalinity is a prerequisite for ooid formation is supported by a few additional lines of evidence. For example, there are a number of documented cases where ooids

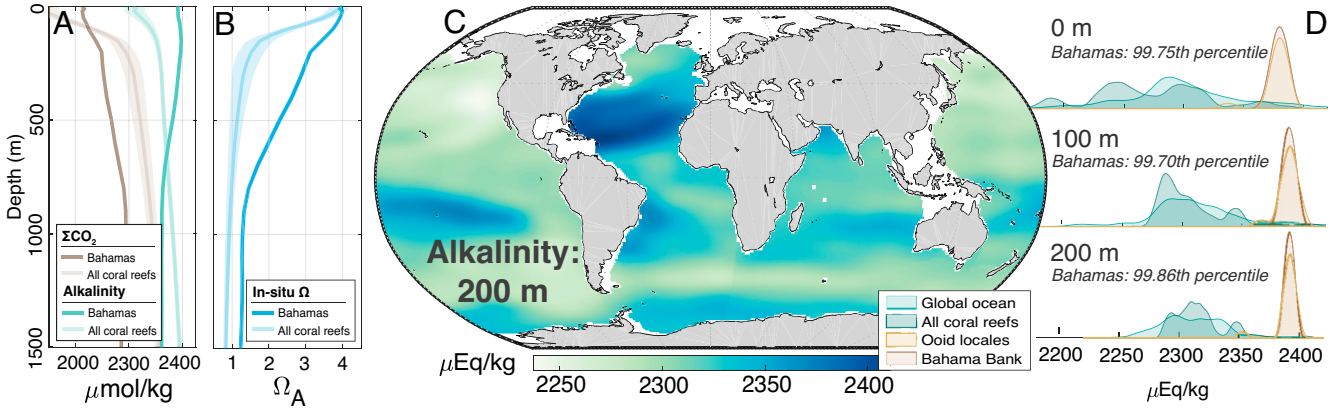

Fig. 7. A possible model for why the Bahama Banks are one of only a few locales in the world to have substantial deposition of nonskeletal carbonate (mud and ooids). (*A* and *B*) The ocean water sourcing the Bahama Banks has high alkalinity and low ΣCO_2 across the upper ~600 m of the water column (58). As a result, Ω_A remains >3 for the upper 250 m of the water column. The "All coral reefs" category uses a global inventory of waters adjacent to shallow coral reefs (*SI Appendix*, Fig. S23). (*C* and *D*) Bahamian seawater has uniquely high alkalinity (>99.7th percentile of all tropical carbonate environments in the modern ocean).

were present earlier in the Holocene—when local climate and ocean currents supported more alkaline conditions—even if they are absent today (60, 62). Also, outside of the west Atlantic, the predominant environments in which ooids form are highly evaporative, alkaline basins, such as Great Salt Lake, Shark Bay, and the Persian Gulf (*SI Appendix*, Fig. S23; ref. 60).

Finally, we must identify the origin of the uniquely alkaline waters reaching the Bahama Banks. Temperature–salinity fingerprinting and output from the Geophysical Fluid Dynamics Laboratory (GFDL) global ocean simulation suggest that the evaporatively enriched Mediterranean Sea is the source of these alkaline waters (Fig. 7*C* and *SI Appendix*, Figs. S28 and S29). To test this Mediterranean–Bahamian teleconnection, we look to the geological record.

A Mediterranean–Bahamian teleconnection? If the vast accumulations of nonskeletal carbonate on the Bahama Banks owe their existence to the salty, alkaline waters of the Mediterranean Basin (Figs. 6*B* and 7*C*), then one prediction is that Bahamian carbonate production should be sensitive to perturbations in Mediterranean outflow. The Messinian salinity crisis (when, at ~5.97 to 5.33 million years ago (Ma), the Mediterranean became isolated from the Atlantic and accumulated evaporite deposits) marks the largest such perturbation (63). Paleoreconstructions of the dimensions of the Atlantic–Mediterranean gateway indicate that Mediterranean outflow was reduced from ~8 to 5.33 Ma (63). Chronostratigraphic age models for the proximal periplatform cores on the western margin of the GBB (64) all show evidence for a ~3-million-year hiatus during this same interval (Fig. 8), which was not caused by sea-level fall (68, 69). In other words, when the enriched alkalinity source to the Bahamas was shut off in the Miocene, Bahamian carbonate production and export were reduced dramatically.

Implications for Shallow Carbonate Production as a Driver of Global Climate. We interpret the case study from the Messinian salinity crisis (Fig. 8) to indicate that nonskeletal carbonate

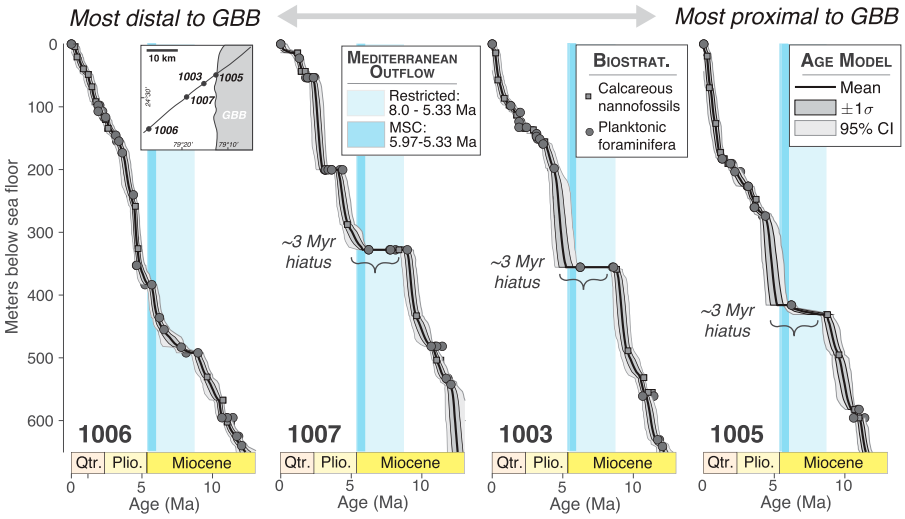

Fig. 8. Mediterranean outflow and Bahamian mud production: a case study from the Messinian salinity crisis. Age models constructed for Bahamian periplatform cores (64) illustrate a prolonged, 3-Myr hiatus concurrent with the reduced dimensions of the Atlantic–Mediterranean gateway (63) (~8 to 5.33 Ma). The nearby cores Clino and Unda show similar evidence for a hiatus (64), but their age models are less constrained due to pervasive Pleistocene meteoric diagenesis and poor microfossil preservation (64, 65). See *SI Appendix* for a description of the MCMC methods used to construct the age models (33). Note that accumulation rates decrease from 1005 to 1007 (proximal to distal), except for the most distal core, 1006, which has a larger pelagic sediment flux (64) and does not experience a hiatus at the Miocene–Pliocene boundary (5.33 Ma). Also, note that the resumption of Mediterranean outflow around 5.33 Ma is associated with an increase in sedimentation rates (*SI Appendix*, Fig. S31) and a shift from a more bioclast-dominated carbonate system to a more mud-dominated system (66). The increase in mud export from the Bahama Banks also is manifested as an increase in $\delta^{13}C$ in the periplatform sites (38, 67), which is opposite to the global open-ocean trend (67), but is consistent with the observation that banktop mud has high $\delta^{13}C$ compared to skeletal and pelagic components (10, 33). Biostrat., biostratigraphy; Plio, Pliocene; Qtr., Quaternary.

production is sensitive to the chemistry of the ambient seawater and to the tectonic, oceanographic, and/or climatic conditions that control it. Next, we ask whether we can draw the arrow the other way—i.e., to what extent does shallow carbonate production not just respond to global climate change, but also drive it?

A simple model of global CO_2 fluxes and carbonate burial. We formulate a simple model to gain first-order insight into how changing the productivity of shallow-water carbonate factories impacts the climate system (70, 71). The alkalinity flux to the ocean from the weathering of both carbonate and silicate minerals (72), $F_{in} = 6.0 \times 10^{13}$ mol $\cdot$ y^{-1}, is balanced primarily by $CaCO_3$ burial on shallow platforms/slopes ($F_{shallow}$, defined following ref. 70 as depths <500 m) and in the deep ocean (F_{deep}) (Fig. 9*A*) (70). In particular, the deep-ocean carbon cycle involves an overproduction of $CaCO_3$ in surface waters, compensated by dissolution of $CaCO_3$ at depth (73). We apply an open-ocean $CaCO_3$ rain rate of 0.89 g $\cdot$ cm^{-2} $\cdot$ y^{-1} (70, 73) and use the modern ocean hypsometry to compute what the steady-state carbonate saturation horizon must be for the net $CaCO_3$ burial flux to balance the alkalinity influx, F_{in} (70). We also make the simplifying assumption that, in the deep box (Fig. 9*A*), all $CaCO_3$ deposited above the calcite saturation horizon is buried, and all $CaCO_3$ deposited below the saturation horizon is dissolved. We note that a more detailed formulation would explicitly describe the shape of the lysocline and the effects of respiration-driven dissolution (including at $\Omega > 1$) (76). For the shallow box, we expect up to 20 to 50% of carbonate to be dissolved (driven by respiration and sulfide oxidation in porewaters) (2, 45). However, we make the assumption that this dissolution is not a function of atmospheric pCO_2, and so we denote $F_{shallow}$ as the net flux (production minus dissolution). In this model framework, the saturation depth in the deep ocean constrains the value of $[CO_3^{2-}]_{deep}$, which, in turn, controls pCO_2 (70) (Fig. 9*B*).

Fig. 9*D* shows that, through the steady-state carbonate compensation mechanism (where the lysocline shoals or deepens to make the net carbonate burial match the alkalinity influx), changing the locus of carbonate burial between the shallow vs. deep ocean leads to a significant ($\geq$150 parts per million [ppm]) change in pCO_2. Additional feedbacks between pCO_2 and ocean temperatures can further amplify the pCO_2 change (*SI Appendix*, Fig. S30). Using the modern carbonate production on the Bahama Banks (30) of 70 Mt $CaCO_3$ y^{-1} [representing 6.65% of the global burial in shallow carbonate environments, or 6.36% of the global deep-sea carbonate sink (2)] as a guide, we estimate that the resumption of Bahamian carbonate production at the end of the Messinian salinity crisis (Fig. 8) could have driven a pCO_2 rise of ~20 ppm, consistent with proxy data suggesting an increase in pCO_2 and sea-surface temperatures at the Miocene–Pliocene boundary (*SI Appendix*, Fig. S31).

The suggestion that changing the locus of carbonate deposition from shallow to deep exerts a first-order control on global pCO_2 (70, 71) (Fig. 9) highlights the importance of understanding the mechanisms of carbonate formation in regions like the Bahamas. For example, in the quest to disentangle the causes of glacial–interglacial CO_2 change (77), it becomes essential that we constrain how much shallow-water carbonate production decreased during glacial lowstands (2, 70). The prevailing view of all shallow-water carbonate being produced on the banktop (36, 49)—whether from corals (2, 70), whiting events (22, 24), green algae (7), ooids (9), etc.—would imply that the shallow carbonate factory would shut off almost completely during glacial periods, when the banktop is exposed. As a result, the shift from ~50% shallow $CaCO_3$ burial in the modern interglacial state (2) to, for example, ~10% shallow $CaCO_3$ burial during glacial lowstands (2), would lower global pCO_2 by ~60 ppm (Fig. 9*D*), but also provoke a change in the carbonate compensation depth

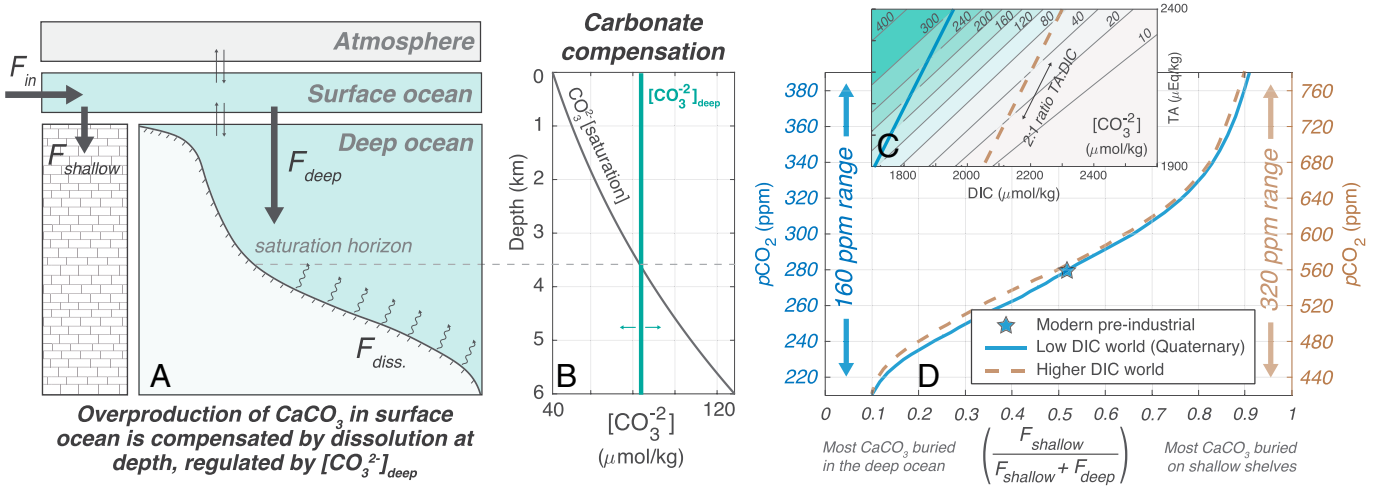

Fig. 9. (*A*) A simple model to explore how changing the fraction of shallow-water carbonate burial affects global pCO_2 (70). The alkalinity influx to the ocean, F_{in}, is balanced by the burial of carbonate in the shallow and deep ocean ($F_{shallow}$ and F_{deep}, respectively) (72, 73). (*B*) The $[CO_3^{2-}]$ content of the deep ocean is relatively invariant with depth (51, 73). However, carbonate's retrograde solubility means that the $[CO_3^{2-}]$ content required for saturation increases with depth (51). The intersection of the $[CO_3^{2-}]_{deep}$ and $[CO_3^{2-}]_{sat}$ curves defines the "saturation horizon." At steady state, the $[CO_3^{2-}]_{deep}$ and saturation horizon adjust such that the net $CaCO_3$ burial balances the influx of alkalinity, F_{in}. Since the mechanism of carbonate compensation changes total alkalinity (TA) and DIC in a 2:1 ratio (51), removing one degree of freedom in the carbonate system, the $[CO_3^{2-}]$ can be used to solve for the remaining parameters of the carbonate system (TA, DIC, pCO_2, etc.) and, therefore, the pCO_2 of the overlying atmosphere (51, 70). (*C* and *D*) We solve for pCO_2 as a function of $f = \left(\frac{F_{shallow}}{F_{shallow}+F_{deep}}\right)$ for two plausible arrays of seawater chemistry (*C*): one representing a relatively low pCO_2 world similar to the Quaternary and one representing a higher pCO_2 world perhaps more representative of the mid-Miocene (74). In both cases, the mechanism of carbonate compensation (*B*) results in the phenomenon that, as a greater fraction of $CaCO_3$ burial occurs on shallow shelves, less carbonate can be buried in the deep ocean, so $[CO_3^{2-}]$ decreases. Lower $[CO_3^{2-}]$ corresponds to higher pCO_2 (51). So, higher f (higher relative $CaCO_3$ burial on shallow shelves compared to the deep ocean) corresponds to higher steady-state atmospheric pCO_2. Because of the hypsometry of the ocean basins and the nonlinear behavior of the CO_2 system in seawater (51), modulating f results in a larger pCO_2 change in the high-DIC world than in the low-DIC world. Note that, in a world without abundant biomineralizers [e.g., the Precambrian (1)], the steady-state alkalinity and Ω required to make the carbonate removal flux match the input flux (F_{in}) may be higher due to the lack of biological carbonate-concentrating mechanisms (12), a change that acts to decrease atmospheric pCO_2 (51, 75). Diss., dissolution.

(CCD) (70) and deep-ocean carbonate burial that is not observed (78). In contrast, we now have evidence to support mud formation on the bank margins that persists through glacial lowstands (Fig. 5*C*), which can help to explain why there is little to no observed change in glacial vs. interglacial CCDs (70, 78).

Predictions for the Anthropocene. If shallow carbonate production is a strong lever on global pCO_2 and climate (Fig. 9), then there is a silver lining for the Anthropocene. The observations of Broecker and Takahashi (30) show that aging banktop waters in the Bahamas maintain pCO_2 equilibrium with the overlying atmosphere (13). As a result, as pCO_2 increases, Ω_A of banktop waters will decrease, and, thus, less $CaCO_3$ can be precipitated from a parcel of seawater before that parcel crosses the threshold for chemical favorability (8, 21, 30, 47, 79). Under current atmospheric pCO_2 of 410 ppm, we estimate that the Bahama Banks only produce half as much carbonate compared to preindustrial conditions of 280 ppm (*SI Appendix*, Fig. S32). By $pCO_2 =$ 1,000 ppm, banktop carbonate production will shut off almost completely* (*SI Appendix*, Fig. S32). Thus, for the modern ocean, there is a negative feedback encoded in Fig. 9; as pCO_2 rises, the shallow carbonate factory becomes less productive, shifting more $CaCO_3$ burial to the deep ocean, which requires an increase in deep ocean $[CO_3^{2-}]$ and a decrease in global pCO_2 (51, 73).

Implications for Mechanisms of Mud Formation in the Past. The Bahamas stand apart as being one of the largest depocenters of shallow carbonate mud in the modern world (15, 16, 21, 29). We recognize that the predominant mud-formation mechanism elsewhere may not be direct precipitation from seawater, as argued here and previously suggested by other workers (8, 21, 30, 47). The fine-grained carbonate in these other, less productive environments may be derived largely from algal disintegration (7, 20, 25) or grain abrasion (9, 26, 28, 29). Yet, the observation that the majority of the mud in the world's largest mud factory is nonskeletal in origin helps alleviate the burden of trying to explain the great quantities of carbonate mudstone that exist prior to the evolution of carbonate biomineralizing organisms (1). Finally, the suggestion that the Bahamian mud factory owes its existence to uniquely favorable (alkaline) waters opens up the possibility that the abundance of nonskeletal muds in the geological record may tell us about paleoalkalinity (Fig. 7) (60), the partitioning of carbonate burial in the shallow vs. deep ocean (70), and, ultimately, pCO_2 (Fig. 9).

Implications for Geochemical Records Derived from Ancient Carbonates. Our results lend cautious support to the practice of targeting rocks made of carbonate mud (micrite) in analyses aimed at reconstructing ancient seawater chemistry. For example, although the $\delta^{13}C$ of Recent carbonates on the Bahama Banks span nearly the full range observed through Earth history (10) (-12 to $+8$‰), the $\delta^{13}C$ value of Recent carbonate mud—regardless of where it is sampled on the bank—remains a relatively faithful recorder of the $\delta^{13}C$ of large-scale oceanic source waters (10). Our framework of bank-margin mud precipitation helps to make sense of the observation of remarkably normal mud $\delta^{13}C$ values within the >15‰ spread of Bahamian carbonates (10): 1) Most mud forms from waters that carry the $\delta^{13}C$ signature of oceanic source waters, rather than of freshwater input (10, 11) or of a strong diurnal carbon engine (13); and 2) Bahamian mud predominantly is not sourced from skeletal components that are prone to substantial $\delta^{13}C$ enrichments and depletions associated with vital effects (12).

Conclusions

The origin of carbonate mud has remained a subject of debate for the last hundred years (8, 9, 18–24, 26, 29). We use geochemical fingerprinting to show that Bahamian mud is not sourced from the breakdown of algae or the abrasion of any possible mixture of macroscopic carbonate constituents (ooids, foraminifera, algae, or corals). Instead, we find evidence for an additional, geochemically distinct aragonitic end-member, which we postulate represents a seawater precipitate. We use clumped isotope thermometry and ocean-temperature observations to show that the measured Δ_{47} temperatures of banktop muds are colder than what would be predicted for formation during whiting events. Instead, we find that the clumped-isotope temperatures are consistent with a model of mud production concentrated on the bank margins and upper slopes. Finally, we explore why the Bahamas are the largest factory of nonskeletal carbonate in the modern world. Our suggestion—that alkaline waters sourced from the Mediterranean conspire with prevailing winds and seafloor topography to produce a uniquely productive carbonate factory—has important implications not only for Mediterranean–Bahamian teleconnections in the global carbon cycle, but also for our understanding of the potentially first-order controls that seawater chemistry and paleogeography play in the carbonate fabrics formed throughout Earth history.

Materials and Methods

Details of the minor- and trace-element, mineralogy, stable isotope, and clumped-isotope analyses are provided in the *SI Appendix*.

Data, Materials, and Software Availability. All geochemical data are available online on Princeton Dataspace (https://doi.org/10.34770/ 0kd8-4233) (80).

ACKNOWLEDGMENTS. This material is based on work supported by NSF Division of Earth Sciences Grant 1410317, the High Meadows Environmental Institute, the Geological Society of America Stephen G. Pollock Student Research Grant, the Evolving Earth Foundation, and the Princeton Geosciences Student Research Fund. E.C.G. thanks the NSF Graduate Research Fellowships Program and the Fannie and John Hertz Foundation. D.A.S. acknowledges support from the U.S. Department of Energy, Office of Science, Office of Basic Energy Sciences, Chemical Sciences, Geosciences, and Biosciences Division, under Award Number DE-AC02-05CH11231. We acknowledge the use of Princeton's Imaging and Analysis Center, which is partially supported through the Princeton Center for Complex Materials, an NSF Materials Research Science and Engineering Centers program (DMR-2011750). We thank Liam O'Connor and Tano Humes for field assistance in the Bahamas. Thank you to John Valley, Jon Husson, Nadir Jeevanjee, Blair Schoene, Amanda Oehlert, Peter Swart, and John Grotzinger for insightful conversation. Linda Kah, Nick Tosca, and an anonymous reviewer provided valuable feedback. Finally, thank you to Jeff Birch, the Small Hope Bay Lodge staff, and the Bahamas Environment, Science & Technology Commission for making work possible on Andros Island.

*Note that these estimates are for modern seawater chemistry; other periods in Earth history could have pCO_2 >1,000 ppm and still maintain abundant shallow carbonate production as long as they had different seawater carbonate chemistry (51) or a smaller deep-ocean carbonate sink (71).

1. M. D. Cantine, A. H. Knoll, K. D. Bergmann, Carbonates before skeletons: A database approach. *Earth Sci. Rev.* **201**, 103065 (2020).
2. J. D. Milliman, Production and accumulation of calcium carbonate in the ocean: Budget of a nonsteady state. *Global Biogeochem. Cycles* **7**, 927–957 (1993).
3. J. D. Milliman, A. W. Droxler, Calcium carbonate sedimentation in the global ocean: Linkages between the neritic and pelagic environments. *Oceanography* **8**, 92–94 (1995).
4. A. Knoll, W. Walter, Latest Proterozoic stratigraphy and Earth history. *Nature* **356**, 673–677 (1992).
5. M. R. Saltzman, E. Thomas, "Carbon isotope stratigraphy" in *Geologic Time Scale 2012*, F. M. Gradstein, J. G. Ogg, M. Schmitz, G. Ogg, Eds. (Elsevier, Amsterdam, 2012), pp. 207–232.
6. K. D. Bergmann, S. A. Al Balushi, T. J. Mackey, J. P. Grotzinger, J. M. Eiler, A 600-million-year carbonate clumped-isotope record from the Sultanate of Oman. *J. Sediment. Res.* **88**, 960–979 (2018).

7. H. A. Lowenstam, S. Epstein, On the origin of sedimentary aragonite needles of the Great Bahama Bank. *J. Geol.* **65**, 364–375 (1957).
8. J. W. Morse, F. J. Millero, V. Thurmond, E. Brown, H. Ostlund, The carbonate chemistry of Grand Bahama Bank waters: After 18 years another look. *J. Geophys. Res. Oceans* **89**, 3604–3614 (1984).
9. E. J. Trower, M. P. Lamb, W. W. Fischer, The origin of carbonate mud. *Geophys. Res. Lett.* **46**, 2696–2703 (2019).
10. E. C. Geyman, A. C. Maloof, Facies control on carbonate $\delta^{13}C$ on the Great Bahama Bank. *Geology* **49**, 1049–1054 (2021).
11. W. Patterson, L. Walter, Depletion of ^{13}C in seawater DIC on modern carbonate platforms: Significance for the carbon isotopic record of carbonates. *Geology* **22**, 885–888 (1994).
12. S. Chen, A. C. Gagnon, J. F. Adkins, Carbonic anhydrase, coral calcification and a new model of stable isotope vital effects. *Geochim. Cosmochim. Acta* **236**, 179–197 (2018).
13. E. Geyman, A. Maloof, A diurnal carbon engine explains ^{13}C-enriched carbonates without increasing the global production of oxygen. *Proc. Natl. Acad. Sci. U.S.A.* **116**, 24433–24439 (2019).
14. L. L. Nelson, A. S. C. Ahm, F. A. Macdonald, J. A. Higgins, E. F. Smith, Fingerprinting local controls on the Neoproterozoic carbon cycle with the isotopic record of Cryogenian carbonates in the Panamint Range, California. *Earth Planet. Sci. Lett.* **566**, 116956 (2021).
15. N. D. Newell, J. K. Rigby, *Geological Studies on the Great Bahama Bank in Regional Aspects of Carbonate Deposition* (SEPM Society for Sedimentary Geology, Broken Arrow, OK, 1957).
16. E. G. Purdy, Recent calcium carbonate facies of the Great Bahama Bank. 2. Sedimentary facies. *J. Geol.* **71**, 472–497 (1963).
17. P. M. Harris, S. J. Purkis, J. Ellis, P. K. Swart, J. J. Reijmer, Mapping bathymetry and depositional facies on Great Bahama Bank. *Sedimentology* **62**, 566–589 (2015).
18. T. W. Vaughan, *Preliminary Remarks on the Geology of the Bahamas with Special Reference to the Origin of the Bahaman and Floridian Oolites* (Papers from the Tortugas Laboratory of the Carnegie Institution of Washington, Carnegie Institution of Washington, Washington, DC, 1914), vol. 5.
19. M. Black, The precipitation of calcium carbonate on the Great Bahama Bank. *Geol. Mag.* **70**, 455–466 (1933).
20. H. A. Lowenstam, Aragonite needles secreted by algae and some sedimentary implications. *J. Sediment. Res.* **25**, 270–272 (1955).
21. P. E. Cloud *et al.*, "Environment of calcium carbonate deposition west of Andros Island, Bahamas" (Tech. Rep., US Government Printing Office, Washington, DC, 1962).
22. E. A. Shinn, R. P. Steinen, B. H. Lidz, P. K. Swart, Whitings, a sedimentologic dilemma. *J. Sediment. Res.* **59**, 147–161 (1989).
23. L. Robbins, P. Blackwelder, Biochemical and ultrastructural evidence for the origin of whitings: A biologically induced calcium carbonate precipitation mechanism. *Geology* **20**, 464–468 (1992).
24. L. Robbins, Y. Tao, C. Evans, Temporal and spatial distribution of whitings on Great Bahama Bank and a new lime mud budget. *Geology* **25**, 947–950 (1997).
25. A. C. Neumann, L. S. Land, Lime mud deposition and calcareous algae in the Bight of Abaco, Bahamas; a budget. *J. Sediment. Res.* **45**, 763–786 (1975).
26. R. Mathews, Genesis of recent lime mud in southern British Honduras. *J. Sediment. Res.* **36**, 428–454 (1966).
27. R. P. Reid, I. G. Macintyre, J. E. Post, Micritized skeletal grains in northern Belize Lagoon; a major source of Mg-calcite mud. *J. Sediment. Res.* **62**, 145–156 (1992).
28. E. Gischler, D. Zingeler, The origin of carbonate mud in isolated carbonate platforms of Belize, Central America. *Int. J. Earth Sci.* **91**, 1054–1070 (2002).
29. E. Gischler, S. Dietrich, D. Harris, J. Webster, R. Ginsburg, A comparative study of modern carbonate mud in reefs and carbonate platforms: Mostly biogenic, some precipitated. *Sediment. Geol.* **292**, 36–55 (2013).
30. W. Broecker, T. Takahashi, Calcium carbonate precipitation on the Bahama Banks. *J. Geophys. Res.* **71**, 1575–1602 (1966).
31. W. Broecker, A. Sanyal, T. Takahashi, The origin of Bahamian whitings revisited. *Geophys. Res. Lett.* **27**, 3759–3760 (2000).
32. S. Purkis *et al.*, Hydrodynamic control of whitings on Great Bahama Bank. *Geology* **45**, 939–942 (2017).
33. S. Edmonsond, A. C. Maloof, "Were shallow carbonate geochemistry and production different during the last interglacial period?" Sr. thesis, Princeton University, Princeton, NJ (2021).
34. J. S. Kier, O. H. Pilkey, The influence of sea level changes on sediment carbonate mineralogy, Tongue of the Ocean, Bahamas. *Mar. Geol.* **11**, 189–200 (1971).
35. A. W. Droxler, J. W. Morse, W. A. Kornicker, Controls on carbonate mineral accumulation in Bahamian basins and adjacent Atlantic Ocean sediments. *J. Sediment. Res.* **58**, 120–130 (1988).
36. J. D. Milliman, D. Freile, R. P. Steinen, R. J. Wilber, Great Bahama Bank aragonitic muds; mostly inorganically precipitated, mostly exported. *J. Sediment. Res.* **63**, 589–595 (1993).
37. J. M. Eiler, Paleoclimate reconstruction using carbonate clumped isotope thermometry. *Quat. Sci. Rev.* **30**, 3575–3588 (2011).
38. A. S. C. Ahm, C. J. Bjerrum, C. L. Blättler, P. K. Swart, J. A. Higgins, Quantifying early marine diagenesis in shallow-water carbonate sediments. *Geochim. Cosmochim. Acta* **236**, 140–159 (2018).
39. J. L. Banner, G. N. Hanson, Calculation of simultaneous isotopic and trace element variations during water-rock interaction with applications to carbonate diagenesis. *Geochim. Cosmochim. Acta* **54**, 3123–3137 (1990).
40. I. G. Macintyre, R. P. Reid, Comment on the origin of aragonite needle mud; a picture is worth a thousand words. *J. Sediment. Res.* **62**, 1095–1097 (1992).
41. S. M. Stanley, J. B. Ries, L. A. Hardie, Seawater chemistry, coccolithophore population growth, and the origin of Cretaceous chalk. *Geology* **33**, 593–596 (2005).
42. S. Husseini, R. Matthews, Distribution of high-magnesium calcite in lime muds of the Great Bahama Bank; diagenetic implications. *J. Sediment. Res.* **42**, 179–182 (1972).
43. J. W. Morse, A. Mucci, Composition of carbonate overgrowths produced on Iceland spar calcite crystals buried in Bahamian carbonate-rich sediments. *Sediment. Geol.* **40**, 287–291 (1984).
44. P. Swart, J. Reijmer, R. Otto, A re-evaluation of facies on Great Bahama Bank II: Variations in the $\delta^{13}C$, $\delta^{18}O$ and mineralogy of surface sediments. *Int. Assoc. Sedimentol. Spec. Publ.* **41**, 47–59 (2009).
45. D. J. Burdige, X. Hu, R. C. Zimmerman, The widespread occurrence of coupled carbonate dissolution/reprecipitation in surface sediments on the Bahamas Bank. *Am. J. Sci.* **310**, 492–521 (2010).
46. M. Rubinson, R. Clayton, Carbon-13 fractionation between aragonite and calcite. *Geochim. Cosmochim. Acta* **33**, 997–1002 (1969).
47. J. W. Morse, D. K. Gledhill, F. J. Millero, $CaCO_3$ precipitation kinetics in waters from the Great Bahama Bank: Implications for the relationship between bank hydrochemistry and whitings. *Geochim. Cosmochim. Acta* **67**, 2819–2826 (2003).
48. W. S. Broecker, C. Langdon, T. Takahashi, T. H. Peng, Factors controlling the rate of $CaCO_3$ precipitation on Great Bahama Bank. *Global Biogeochem. Cycles* **15**, 589–596 (2001).
49. M. R. Boardman, A. C. Neumann, Sources of periplatform carbonates; Northwest Providence Channel, Bahamas. *J. Sediment. Res.* **54**, 1110–1123 (1984).
50. G. M. Grammer *et al.*, Rapid growth rates of syndepositional marine aragonite cements in steep marginal slope deposits, Bahamas and Belize. *J. Sediment. Res.* **63**, 983–989 (1993).
51. R. E. Zeebe, D. Wolf-Gladrow, *CO_2 in Seawater: Equilibrium, Kinetics, Isotopes* (Gulf Professional Publishing, Houston, 2001).
52. C. S. Romanek, J. W. Morse, E. L. Grossman, Aragonite kinetics in dilute solutions. *Aquat. Geochem.* **17**, 339–356 (2011).
53. P. W. Reiners *et al.*, *Geochronology and Thermochronology* (John Wiley & Sons, Hoboken, NJ, 2017).
54. N. Anderson *et al.*, A unified clumped isotope thermometer calibration (0.5–1,100 c) using carbonate-based standardization. *Geophys. Res. Lett.* **48**, e2020GL092069 (2021).
55. E. C. Geyman, A. C. Maloof, B. Dyer, How is sea level change encoded in carbonate stratigraphy? *Earth Planet. Sci. Lett.* **560**, 116790 (2021).
56. E. A. Burton, L. M. Walter, Relative precipitation rates of aragonite and Mg calcite from seawater: Temperature or carbonate ion control? *Geology* **15**, 111–114 (1987).
57. S. Roest-Ellis, J. V. Strauss, N. J. Tosca, Experimental constraints on nonskeletal $CaCO_3$ precipitation from Proterozoic seawater. *Geology* **49**, 561–565 (2021).
58. R. M. Key *et al.*, A global ocean carbon climatology: Results from Global Data Analysis Project (GLODAP). *Global Biogeochem. Cycles* **18**, GB4031 (2004).
59. E. C. Rankey, S. L. Reeder, Holocene ooids of Aitutaki Atoll, Cook Islands, South Pacific. *Geology* **37**, 971–974 (2009).
60. S. Gallagher *et al.*, The enigma of rare Quaternary oolites in the Indian and Pacific Oceans: A result of global oceanographic physicochemical conditions or a sampling bias? *Quat. Sci. Rev.* **200**, 114–122 (2018).
61. M. Laugié, J. Michel, A. Pohl, E. Poli, J. Borgomano, Global distribution of modern shallow-water marine carbonate factories: A spatial model based on environmental parameters. *Sci. Rep.* **9**, 1–14 (2019).
62. M. Hallenberger *et al.*, Increased fluvial runoff terminated inorganic aragonite precipitation on the Northwest Shelf of Australia during the early Holocene. *Sci. Rep.* **9**, 18356 (2019).
63. W. Capella *et al.*, Mediterranean isolation preconditioning the Earth System for late Miocene climate cooling. *Sci. Rep.* **9**, 3795 (2019).
64. G. Eberli *et al.*, "Bahamas transect (initial reports)" in *Proceedings of the Ocean Drilling Program (ODP)*, G. P. Eberli, P. K. Swart, M. J. Malone, et al., Eds. (Texas A&M University, College Station, TX, 1997), vol. 166, pp. 23–41.
65. B. H. Lidz, T. J. Bralower, Microfossil biostratigraphy of prograding Neogene platform-margin carbonates, Bahamas: Age constraints and alternatives. *Mar. Micropaleontol.* **23**, 265–344 (1994).
66. J. J. Reijmer, C. Betzler, D. Kroon, R. Tiedemann, G. P. Eberli, Bahamian carbonate platform development in response to sea-level changes and the closure of the Isthmus of Panama. *Int. J. Earth Sci.* **91**, 482–489 (2002).
67. P. K. Swart, Global synchronous changes in the carbon isotopic composition of carbonate sediments unrelated to changes in the global carbon cycle. *Proc. Natl. Acad. Sci. U.S.A.* **105**, 13741–13745 (2008).
68. A. M. Oehlert, P. K. Swart, Interpreting carbonate and organic carbon isotope covariance in the sedimentary record. *Nat. Commun.* **5**, 4672 (2014).
69. M. E. Smith, P. K. Swart, The influence of diagenesis on carbon and oxygen isotope values in shallow water carbonates from the Atlantic and Pacific: Implications for the interpretation of the global carbon cycle. *Sediment. Geol.* **434**, 106147 (2022).
70. B. N. Opdyke, J. C. Walker, Return of the coral reef hypothesis: Basin to shelf partitioning of $CaCO_3$ and its effect on atmospheric CO_2. *Geology* **20**, 733–736 (1992).
71. A. Ridgwell, A Mid Mesozoic Revolution in the regulation of ocean chemistry. *Mar. Geol.* **217**, 339–357 (2005).
72. J. J. Middelburg, K. Soetaert, M. Hagens, Ocean alkalinity, buffering and biogeochemical processes. *Rev. Geophys.* **58**, e2019RG000681 (2020).
73. W. Broecker, T. Peng, *Tracers in the Sea* (Eldigio Press, New York, 1982).
74. G. L. Foster, D. L. Royer, D. J. Lunt, Future climate forcing potentially without precedent in the last 420 million years. *Nat. Commun.* **8**, 14845 (2017).
75. J. V. Strauss, N. J. Tosca, Mineralogical constraints on Neoproterozoic pCO_2 and marine carbonate chemistry. *Geology* **48**, 599–603 (2020).
76. D. Archer, Modeling the calcite lysocline. *J. Geophys. Res. Oceans* **96**, 17037–17050 (1991).
77. K. E. Kohfeld, A. Ridgwell, Glacial-interglacial variability in atmospheric CO_2. *Surf. Ocean Low. Atmos. Process.* **187**, 251–286 (2009).
78. N. R. Catubig *et al.*, Global deep-sea burial rate of calcium carbonate during the Last Glacial Maximum. *Paleoceanography* **13**, 298–310 (1998).
79. H. Bustos-Serrano, J. W. Morse, F. J. Millero, The formation of whitings on the Little Bahama Bank. *Mar. Chem.* **113**, 1–8 (2009).
80. E. C. Geyman et al., Data for: "The origin of non-skeletal carbonate mud and implications for global climate." Princeton University DataSpace. https://dataspace.princeton.edu/handle/88435/dsp01xd07gw85q. Deposited 16 June 2022.